crystals

MDPI

Article

Thermodynamic Assessment of Reactions in the Sodium-Oxide Fluxed Aluminothermic Reduction of Manganese Ore with Si, Cr, and Cu Collector Metals

Theresa Coetsee [1,*] and Frederik De Bruin [2]

[1] Department of Materials Science and Metallurgical Engineering, University of Pretoria, Pretoria 0002, South Africa
[2] Independent Metallurgical Consultant, Pretoria 0002, South Africa; fjdb.1953@gmail.com
* Correspondence: theresa.coetsee@up.ac.za

Abstract

This study investigates the reaction thermodynamics of the sodium oxide-fluxed aluminothermic reduction of pyrolusite-based manganese ore under self-propagating high-temperature synthesis (SHS) conditions, using Si, Cr, and Cu as collector metals. The experimental results are compared with thermochemical equilibrium calculations using FactSage 7.3 thermochemistry software. Experimental mixtures were prepared with controlled additions of aluminium, sodium silicate, calcium oxide, and collector metals and heated to the ignition temperature in a muffle furnace preheated to 1350 °C. The resulting alloys and slags were analysed for bulk composition. Collector metals significantly influence alloy carbon saturation and manganese recovery. The individual reaction's Gibbs free energy values and the gas–slag–metal equilibrium were calculated. Discrepancies between the experimental and equilibrium-predicted results highlight the kinetic factors of SHS processes, particularly with respect to aluminium uptake and manganese volatilisation. The main difference is the alloy's aluminium uptake. The difference between the calculated and experimental aluminium levels is, in part, due to the higher partial oxygen pressure predicted in the gas–slag–metal equilibrium calculations, compared with that of the likely Al–Al_2O_3 governing reaction equilibrium. Short-circuiting of aluminium to the alloy is also a possible contributing factor. The findings provide insights into optimising feed formulations and process parameters for improved manganese recovery.

Keywords: aluminothermic; thermodynamics; manganese ore; reduction; slag; collector

Academic Editor: Heinz-Günter Brokmeier

Received: 14 January 2026
Revised: 31 January 2026
Accepted: 4 February 2026
Published: 6 February 2026

1. Introduction

The application of aluminothermy has attracted increased research interest because the aluminium reductant can be recycled from the produced slag back into the Hall–Héroult electrochemical process [1–3]. Various minerals and waste streams are processed with aluminothermy to produce end-products such as steel from mill scale and scheelite concentrate [4–6], Al-Mn-Si alloys from industrial manganese slag and aluminium dross [7,8], Si-Al-Ca alloys from CaO-SiO_2 slag [9,10], ferro-titanium from ilmenite and bauxite residue [3], and low-carbon ferro-manganese from pre-roasted MnO_2 ore [11], as well as to recycle of end-of-life lithium-ion batteries [12]. Complex aluminium-containing alloys are also applied as a reductant in aluminothermy to produce Fe-Mn-Cr ferro-alloys from low-grade chromium and manganese ores [13]. Laboratory studies are typically conducted under an Argon atmosphere in an induction or tube furnace [3,7–10,12]. An

oxygen source such as $NaClO_3$ may be added to the mixture to control aluminium combustion [3]. In contrast, real-life aluminothermy occurs in air under SHS (self-propagating high-temperature synthesis) process conditions [4–6,11,14,15]. The particle size of the aluminium reductant determines the rate of the aluminium combustion reaction and, consequently, the maximum process temperature, metal yield, and final phase chemistries in the slag and alloy products [14,16]. It was found that MnO_2-Al mixtures did not react under Argon and required air and aluminium additions in excess of the reaction stoichiometric ratio to react significantly [17]. Although Beketov pioneered the aluminothermic reduction process in 1859 [18], variations in its application continue to be developed and studied, as evidenced by the above-referenced materials. This is especially the case when aluminium consumption must be optimised to limit the alloying content under SHS process conditions.

Recent work has shown that $NaAlO_2$ is water-soluble and can facilitate the recycling of Al_2O_3 to the Hall–Héroult electrochemical process via the Bayer process. Therefore, a sodium-fluxed formulation was applied in the aluminothermic reduction of MnO_2 ore [19–21]. A small quantity of coal was added to eliminate the pre-roasting step required before the aluminothermic reduction of MnO_2 ore and to avoid the violent, fast heat release from the MnO_2-Al reaction [11]. Different collector metals were applied to increase the alloy yield. The aluminothermic reduction under SHS conditions is unlikely to reach chemical equilibrium because rapid heat release yields short reaction times, thereby limiting the time for product diffusion to form homogeneous equilibrium phases [15]. For example, the encapsulation of reactant aluminium particles within the product was observed during the SHS reaction of SiO_2-MnO_2-Fe-Al mixtures [22]. Alumina product layer formation may also interfere with reaction equilibrium, even though studies of pure MgO-Al mixtures identified an easily breakable alumina product layer that did not hinder further reaction [23].

If the aluminothermic reduction process approaches equilibrium at the high temperatures typically achieved, equilibrium conditions can be used to calculate new formulations, thereby reducing the extent of the required experimental work. This approach was illustrated by metal–slag equilibrium simulations used to specify feed mixtures and to explain experimental results [3,7–10,13]. Despite the use of equilibrium calculations, empirical studies of reaction systems remain necessary. For example, in the formulation of flux materials for self-shielded flux-cored arc welding (FCAW–S), aluminothermic reduction of oxides such as MnO_2, CuO, and Fe_2O_3 is carefully applied to add additional heat to the weld pool [24–26]. Similarly, aluminium is added to improve element transfer efficiency in submerged arc welding (SAW) and requires experimental verification [27].

The objective of this work is the evaluation of the reaction thermodynamics in the sodium-oxide fluxed aluminothermic reduction of MnO_2 ore under SHS process conditions. The experimental results from [18–20] are compared with thermochemical calculations performed in FactSage 7.3 and the differences are discussed [28].

2. Materials and Methods

2.1. Materials

The experimental details used to generate the alloy and slag samples that form the basis of the thermochemical analysis in this work were previously reported [19–21]. Here, the analyses of the input materials and the applied mixtures are repeated for clarity.

The manganese ore is pyrolusite (MnO_2)-based and is sourced from a small-scale ore body complex in South Africa; the medium-volatile coal is also sourced from South Africa. The coal contains 22.5% volatile matter, 12% ash, 62.2% fixed carbon, and 3.3% moisture. Table 1 presents the analyses of the ore and coal ash. The mixture, based on 100 g of ore, was placed in a graphite crucible (SGL Carbon (Pty) Ltd, Johannesburg, South Africa),

sealed with a graphite lid, and heated in a muffle furnace (Gallenkamp, Manchester, UK) preheated to 1350 °C. The reaction mixtures are summarised in Table 2. The feed mixture was designed to contain a limited amount of carbon reductant to facilitate the reduction of ore minerals, specifically FeO(OH) and MnO_2, to FeO and MnO, thereby eliminating the need for a pre-roasting step in the aluminothermic reduction of MnO_2-type ore [11]. The added aluminium mass of 30 g per 100 g of ore represents an 8.5% excess of Al that is required to reduce all Fe_2O_3 and Mn_2O_3 to Fe and Mn. The introduction of Si and Cr as collector metals enables these elements to serve as co-reductants for aluminium.

Table 1. Bulk chemical composition of manganese ore and coal ash (mass%).

	%FeO	%MnO	%Cr_2O_3	%V_2O_5	%TiO_2	%CaO	%K_2O	%P_2O_5	%SiO_2	%Al_2O_3	%MgO	%Na_2O	%BaO
Ore	10.70	61.59	0.03	0.04	0.05	0.23	0.21	0.01	5.43	2.61	0.11	0.00	1.85
Ash	1.51	0.02	0.05	0.05	2.16	2.46	0.51	1.19	51.44	39.35	0.68	0.30	0.27

Table 2. Reaction mixtures (grams).

Mixture	Ore	Coal	$Na_2O.SiO_2$	CaO	Al	Cu	Si	Cr
A	100	10	20	15	30	0	0	0
B	100	10	20	15	30	10	0	0
C	100	10	20	15	30	0	10	0
D	100	10	20	15	30	0	0	10

2.2. Thermochemical Calculations

Gibbs free energy values for the individual reactions in Sections 4.1 and 4.2 were calculated in the Reaction module of FactSage 7.3 using only the temperatures as inputs, with the FToxid, SGTE, and FactPS databases [28]. The gas–slag–metal (g–s–m) equilibrium calculations in Section 4.3 were performed in the Equilib module, using the FToxid, SGTE, and FactPS databases [28]. The stability diagrams in Section 4.3 were calculated in the Phase diagram module using the FToxid, SGTE, and FactPS databases.

The Equilib module's free energy minimisation routine calculates the equilibrium gas, slag, and metal compositions for the user-specified inputs of temperature and the chemistries and mass proportions of ore, fluxes ($Na_2O.SiO_2$, CaO), collector metal, and coal carbon. Therefore, the system was modelled as a closed system, excluding atmospheric air and the crucible graphite, which were not represented in the calculations.

3. Results

The bulk slag and alloy compositions from each reaction mixture are summarised in Tables 3 and 4. The alloy's carbon content is undersaturated, despite the use of graphite crucibles as the mixture containers. For example, the alloy carbon saturation levels at 1650 °C to 1900 °C are 6.8% to 7.4% C in alloy A, 3.6% to 4.5% C in alloy B, 4.5% to 5.2% C in alloy C and 7.2 to 8.1%C in alloy D. It is well known that increased silicon in manganese alloys decreases the carbon saturation level [29]. Copper has a similar effect when added to manganese alloys [30]. The aluminium content of the alloy ranged from 0.4% for sample A to 2.6% in sample B.

Table 3. Bulk chemistry of alloys (mass%).

Mixture	%Al	%Si	%Mn	%Fe	%Cr	%S	%C	%Cu
A	0.4	1.4	66.1	28.0	0	0.03	3.5	0
B	2.6	2.1	53.9	19.1	0	0.10	1.2	20.8
C	1.4	8.7	65.8	21.8	0	0.08	2.2	0
D	1.5	3.4	56.8	18.2	17.7	0.12	2.2	0

Table 4. Bulk chemistry of slags (mass%).

Mixture	%Al_2O_3	%SiO_2	%MnO	%CaO	%Na_2O	%BaO	B2 = %CaO/%SiO_2
Target slag	39	17	14	17	11	2	1.0
A	52.1	11.9	22.7	7.0	4.5	1.5	0.6
B	52.3	11.4	19.4	9.8	5.2	1.5	0.9
C	49.0	21.9	12.6	8.7	6.1	1.3	0.4
D	54.7	10.7	17.5	10.0	5.1	1.6	0.9

The slag analyses obtained in the experiments differ from the target slag analysis in that they contain more Al_2O_3 and less CaO and Na_2O. The higher silica content in mixture C is due to the oxidation of Si to SiO_2, as Si serves as a co-reductant to aluminium. The absence of iron oxides in the slags confirms the complete metallisation of iron oxides, as expected under the highly reducing conditions imposed by the aluminium reductant.

The slag %MnO comparison in Table 4 may be misleading, particularly for mixture C in which SiO_2 was added from the reaction of Si as a reductant. Therefore, the manganese performance numbers are summarised in Table 5. The numbers in Table 5 indicate the highest alloy bulk coalescence in mixtures B and D, as evidenced by the mass of alloy removed from the crucible bottom under the heading "Mn in weighed alloy". The proportion of alloy entrapped in the slag is least in mixtures A and B, and worst in mixture C, likely due to higher slag viscosity from increased SiO_2 in slag C. The best overall Mn recovery in the alloy is observed in mixtures C and D, at 51% and 53%, respectively. The %Mn accounting number represents the mass of manganese accounted for in the slag and alloy, thereby indicating significant gas–phase manganese loss due to vaporisation. The overall alloy yield follows the same trend as the %Mn accounting numbers.

Table 5. Manganese mass distribution among slag and alloy (grams unless otherwise indicated).

Mixture	Alloy Weighed	Mn in Weighed Alloy	Alloy in Slag	Mn in Alloy in Slag	%Mn to Alloy	Mn as MnO in Slag	Mn in Feed Mixture	%Mn Accounting	%Alloy Yield
A	18.7	12.4	5.3	3.5	33	16	48.0	67	43
B	28.6	15.4	8.8	4.7	42	14	48.0	72	57
C	19.2	12.6	18.0	11.8	51	11	48.0	74	56
D	30.6	17.4	13.9	7.9	53	14	48.0	82	68

4. Discussion

The following discussion is organised in three sections, each section examines the reaction system thermodynamics in increased detail. The individual reactions are compared to illustrate the thermodynamically most-favoured (TMF) reactions in different scenarios of compound activity levels. In Section 4.1, the simplest scenario for individual reaction thermodynamics is considered, with pure reactants and products at unit activity.

In Section 4.2, individual reaction thermodynamics is considered for the activities of the endpoint slag and alloy compounds, as calculated in the Equilib module of FactSage 7.3, for the alloy and slag endpoint compositions shown in Tables 3 and 4. Two scenarios are considered. The first scenario is the worst-case scenario for the progression of reduction reactions to completion, since both the reactant and product activities are set equal to those of the endpoint slag and alloy compositions. The second scenario is the most favourable for progressing reduction reactions to completion, as the reactant activities are set to unity and the product activities are set equal to those of the endpoint slag and alloy compositions. This scenario more accurately represents the onset of the reduction process.

Section 4.3 presents the gas–slag–metal (g–s–m) equilibrium results calculated using the free energy minimisation routine in the Equilib module of FactSage 7.3. The equilibrium alloy and slag compositions are compared to the experimental results in Tables 3 and 4.

4.1. Reduction Potential

In considering the relative reductant strength of aluminium, silicon, chromium, and carbon to metallise MnO according to Reactions (1)–(4), the simplified standard Gibbs free energy graph for the reduction reactions is shown in Figure 1 for pure reactants and products (activities equal to 1.0). It is seen that Al, Si, and C can reduce MnO in the temperature range of 1600 °C to 2000 °C. At 1900 °C, MnO reduction by C becomes more favoured than MnO reduction by Si. Any Al consumed as a reductant cannot be regenerated, since Al has the highest reductant strength among Al, Si, and C. In contrast, Si consumed as reductant to form SiO_2 can be regenerated via Al and C reduction of SiO_2 to form Si, according to Reactions (5) and (6). Si loss as SiO gas is more likely at temperatures greater than about 1900 °C, as Reaction (8) becomes more favourable than Reaction (6). The standard Gibbs free energy line for the reduction of MnO by Cr is close to zero, indicating that Reaction (3) may become favourable at lower product activities. Reactions (1), (2), and (4) are the most-favoured MnO reduction reactions in Figure 1, and are considered further in Section 4.2, together with Reaction (3) for Cr as an MnO reductant. Reaction (6) is also considered to test the conditions for regeneration of the Si reductant by carbon reduction.

$$3/2(MnO) + (Al) = 3/2(Mn) + 1/2(Al_2O_3) \quad (1)$$

$$2(MnO) + (Si) = 2(Mn) + (SiO_2) \quad (2)$$

$$(MnO) + (Cr) = (Mn) + (CrO) \quad (3)$$

$$(MnO) + <C> = (Mn) + [CO] \quad (4)$$

$$3/4(SiO_2) + (Al) = 3/4(Si) + 1/2(Al_2O_3) \quad (5)$$

$$1/2(SiO_2) + <C> = 1/2(Si) + [CO] \quad (6)$$

$$1/3(Al_2O_3) + <C> = 2/3(Al) + [CO] \quad (7)$$

$$(SiO_2) + <C> = [SiO] + [CO] \quad (8)$$

< > = solid; ( ) = liquid; [ ] = gas.

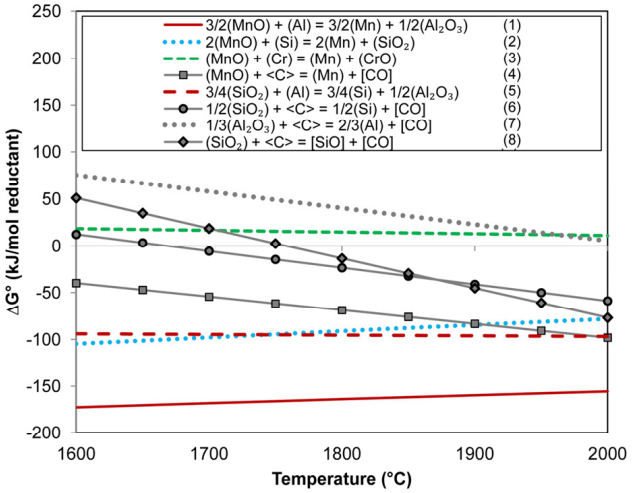

Figure 1. Standard Gibbs free energy of reduction reactions at unit activities.

4.2. Endpoint Composition Activities

For impure compounds in the alloy and slag solution phases, the real activity values must be used to adjust the standard Gibbs free energy from pure compounds to molten impure compounds according to Equation (9). The worst-case scenario in terms of each reaction's Gibbs free energy is found if the endpoint alloy and slag activity values are those when the reactions are closest to equilibrium. The endpoint activities were calculated in FactSage 7.3 using the Equilib module with the endpoint alloy or slag composition as input, individually. The activity values are shown in Figure 2 and summarised in Appendix A.

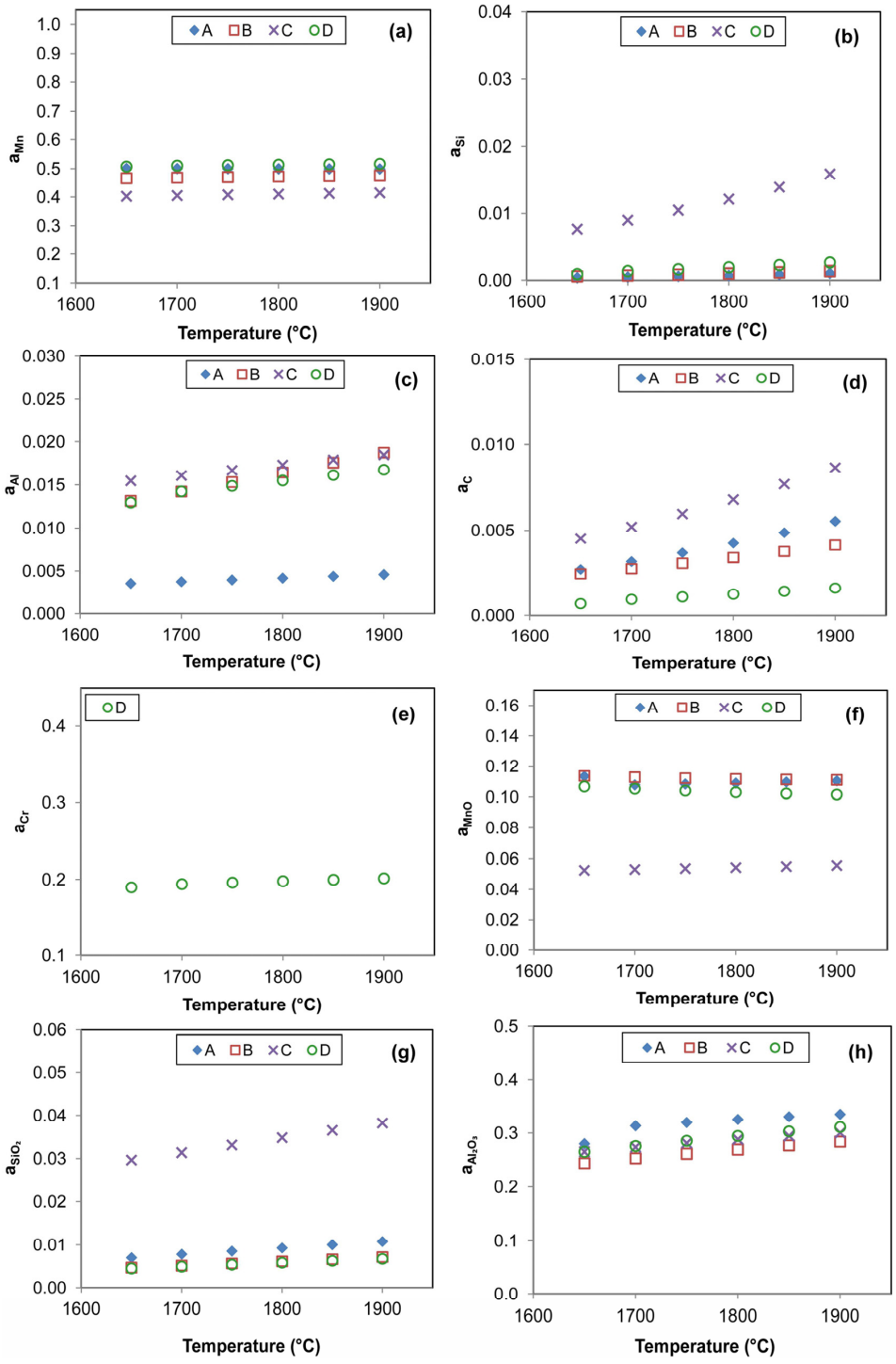

Figure 2. Activity values in experimental endpoint alloy and slag versus temperature: (**a**) Mn; (**b**) Si; (**c**) Al; (**d**) C; (**e**) Cr; (**f**) MnO; (**g**) SiO_2; (**h**) Al_2O_3.

The reaction Gibbs free energy values for the impure endpoint compounds in the slag and alloy, calculated from Equation (9), are shown for each feed mixture as Figure 3a–d, marked with circle icons. In addition, the reaction Gibbs free energy values were calculated for the most favourable scenario, with product activities as in Figure 2 (and Appendix A) and reactant activities set to unity and shown as lines marked with a diamond icons in Figure 3a–d.

$$\Delta G = \Delta G^{\circ} + RTlnK \quad (9)$$

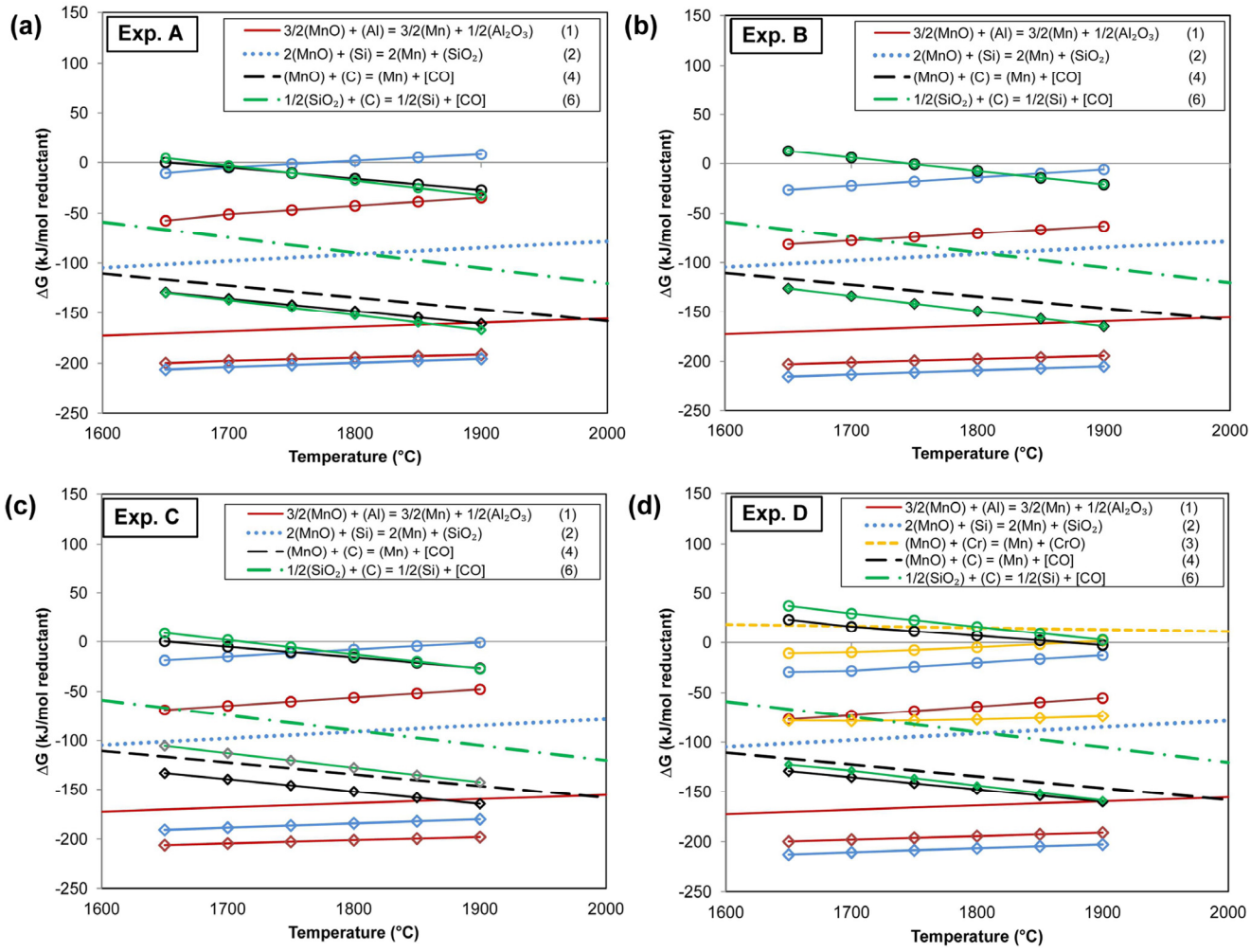

Figure 3. Gibbs free energy values adjusted for impure compounds in alloy and slag. Lines without icons = unit activity in reactants and products; circles = endpoint composition activities; diamonds = reactants at unit activity and products at endpoint composition activities. (**a**) sample A; (**b**) sample B; (**c**) sample C; (**d**) sample D.

For example, in the case of Reaction (1), the following expression in Equation (10) was applied. Appendix B, Table A5, shows the ΔG, ΔG°, and K values for Reaction (1) as applied to the sample A activity values in Table A1, Appendix A.

$$\Delta G = \Delta G^{\circ} + RTln\left(\frac{(a_{Mn})^{1.5}\ (a_{Al_2O_3})^{0.5}}{(a_{MnO})^{1.5}\ (a_{Al})}\right) \quad (10)$$

Figure 3a–d displays the same ΔG° lines for Reactions (1)–(3) as in Figure 1, as reference lines. For Reactions (4) and (6) based on a carbon reductant, the solid carbon expression of Reactions (4) and (6) was changed to dissolved carbon. The value of P_{CO} is set to

1 atmosphere. The reaction Gibbs free energy lines for the worst-case scenario are depicted as circle icons and were calculated by applying the activity values of the endpoint slag and alloy compositions to Equation (9). The reaction Gibbs free energy lines for the most favourable scenario are depicted by diamond icons and were calculated by applying unit activities to the reactants and the activity values of the endpoint slag and alloy compositions to the products in Equation (9).

It is seen that for the unit activities of the reactants and products, Reaction (1) is the TMF (thermodynamically most-favoured) reaction at 1600 °C to 1970 °C. Beyond 1970 °C, Reaction (4) becomes the TMF reaction. The second most-favoured reaction over the considered temperature range is Reaction (4). Reaction (2) is the third most-favoured reaction at 1600 °C to 1800 °C, and is replaced by Reaction (6) at temperatures higher than 1800 °C.

For sample A under the worst-case scenario (circle icons), the Gibbs free energy values of Reactions (1), (4), and (6) in Figure 3a are similar at 1900 °C, at −34 kJ/mol Al, −27 kJ/mol Mn and −32 kJ/mol C. The value for Reaction (2) is positive at eight kJ/mol Si, indicating that this reaction will not proceed at 1900 °C. The relative values are important for the possible reaction mechanisms because they indicate at which temperatures the reduction reactions with carbon, Reactions (4) and (6), are more favoured than the reduction with Si, Reaction (2). Only considering simplified reaction thermodynamics would imply that Reaction (2) is simply the sum of Reaction (4) and the reverse version of Reaction (6). However, no specific insights would be gained from this simplification. This is because, as shown in the above discussion, each reaction of the separate reductants, silicon and carbon, must be considered, as in Reactions (4), (6) and (2).

In contrast to the endpoint activity-based Gibbs free energy lines, for the most favourable activity conditions marked as lines with diamond icons, it is seen that the line for Reaction (2) with the Si reductant is favoured most, but positioned close to the Reaction (1) line. Carbon reduction reactions are similar in Gibbs free energy values, but much less favoured than Reactions (1) and (2). The same trends are observed in Figure 3b, but the crossover temperature between Reactions (2) and (4) with Reaction (6) shifts upward from 1700 °C to 1850 °C. Figure 3c shows the crossover temperature as 1775 °C. The most favourable activity scenario lines of Reactions (4) and (6) are separated in Figure 3c, unlike those in Figure 3a,b,d. The values of Reaction (4) are lower than those of Reaction (6). This is due to lower Mn activity in the endpoint alloy, resulting from the higher silicon content of the sample C feed mixture, as seen in Figure 2a. The shift to more positive Gibbs free energy values of Reaction (2) is due to an increase in silica activity from higher silica content in the sample C slag, as seen in Figure 2g.

Figure 3d indicates positive Gibbs free energy values for Reactions (4) and (6) at the endpoint activity values. Therefore, these two reactions are not important in the endpoint scenario, as they cannot proceed in the forward direction. Chromium has a lower affinity for oxygen than Mn and Si and is therefore not a significant contributor to reduction reactions in this system [31]. This was confirmed by the absence of Cr oxides in slag D [20]. To calculate Gibbs free energy values for Reaction (3) in the absence of chromium oxide in the experimental slag, the activity values of CrO from the gas–slag–metal equilibrium calculations were used. In Figure 3d, the Reaction (3) Gibbs free energy values are positive above 1850 °C at the endpoint composition activity values, confirming that Reaction (3) will not proceed to the product side under such conditions. Reaction (3) may proceed at temperatures below 1850 °C. Under the most favourable activity conditions, Reaction (3) is possible at 1650 °C to 1900 °C due to the slag's low chromium oxide content and the resulting low activity of CrO.

The above discussion shows that limited insight is gained by considering the reaction Gibbs free energy values of the individual reactions in Figure 3a–d because scenario assumptions are applied. Therefore, the gas–slag–metal (g–s–m) equilibrium calculation is often considered the best simulation tool for complex reaction systems. Section 4.3 displays the calculation results and explains the differences between the experimental slag and alloy compositions and the equilibrium calculation values.

4.3. Gas–Slag–Metal Equilibrium

The reaction system was simulated using the gas–slag–metal (g–s–m) equilibrium at different temperatures to determine the likely bulk temperatures achieved. The differences between the experimental alloy and slag analyses and those predicted by chemical equilibrium are considered. The results are summarised in Figure 4a–e, which compare the equilibrium alloy analyses with the experimental analyses in Table 3. Similarly, the slag compositions in Figure 5a–e show the equilibrium slag compositions compared to the experimental results in Table 4. Figure 5f displays the main gas species from the equilibrium calculations, consisting of CO, Na, H_2 and Mn, with SiO also predicted in sample C with silicon metal addition.

The temperature interval of 1650 °C to 1900 °C stems from prior simulation runs made over a wider temperature range in which it was found that simulations above 2500 °C result in total vaporisation of the alloy, and for temperatures below 1600 °C, the predicted alloy carbon content is excessive due to more reducing conditions prevailing at lower temperatures. In comparison, the adiabatic temperature (AT) values are summarised in Table 6 for different input material pre-heating conditions. It is seen that the condition of no pre-heating results in excessive AT values higher than 3000 °C. More realistic AT values are obtained for pre-heating to 700 °C at 1885–1933 °C, and for pre-heating to 1000 °C, the AT values range from 1959 to 1992 °C. The AT values are sufficiently high to ensure the SHS conditions prevail in the reaction system [14,22]. From the AT values in Table 6, it is seen that the temperature interval of 1650 °C to 1900 °C is realistic in terms of the g–s–m equilibrium calculations.

Table 6. Adiabatic temperatures (AT) in °C versus input material pre-heating temperature.

Mixture	No Pre-Heating	Pre-Heating to 700 °C	Pre-Heating to 1000 °C
A	3366	1885	1959
B	3333	1880	1964
C	3290	1933	1992
D	3322	1900	1972

The g–s–m equilibrium calculations do not accurately predict the alloy aluminium content, as they predict almost complete aluminium reaction to Al_2O_3 via Reaction (1). The alloy aluminium analyses versus the low equilibrium-predicted values in Figure 4a, and the opposite predicted trend versus experimentally measured alloy manganese levels in Figure 4d, show this discrepancy from equilibrium. Consequently, the slag equilibrium compositions have a lower %MnO and a higher %Al_2O_3 than the experimentally measured values, as in Figure 5a,b.

Figure 4c illustrates the trend in the predicted carbon content of the alloy. It is seen that the temperatures at which the experimental and equilibrium carbon contents overlap are at 1650 °C to 1700 °C for sample A, 1700 °C to 1750 °C for sample B, 1700 °C for sample C, and 1800 °C to 1850 °C for sample D. In the case of samples A, B, and D, the silicon content matching temperatures are similar to those of the carbon content, see Figure 4b. A large discrepancy exists between the experimental and predicted silicon content of sample

C, due to lower silicon uptake into the alloy and greater SiO_2 in the slag than predicted by equilibrium calculations.

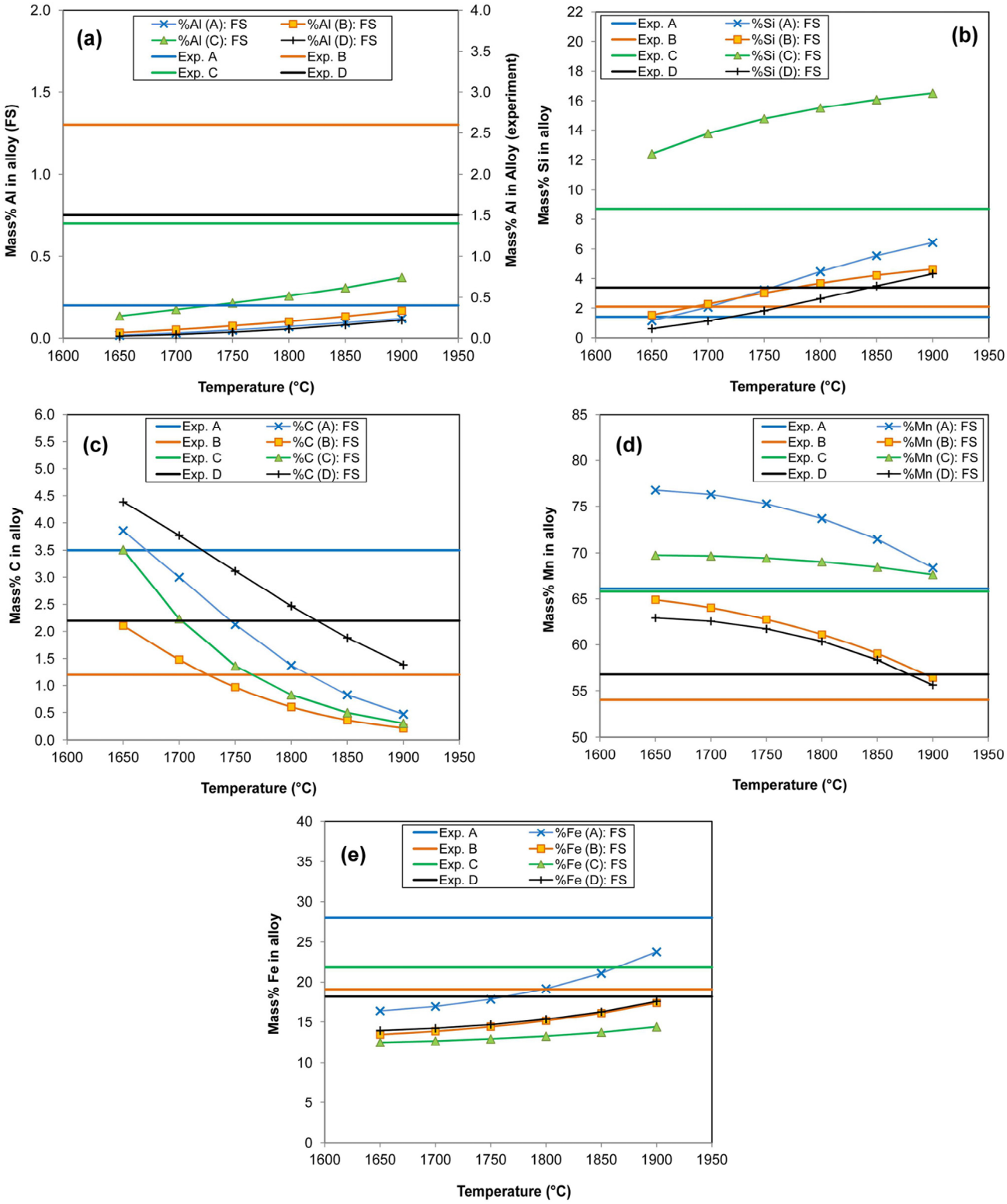

Figure 4. Gas–slag–metal equilibrium compositions of the alloy phase vs. experiment. (**a**) Al; (**b**) Si; (**c**) C; (**d**) Mn; (**e**) Fe.

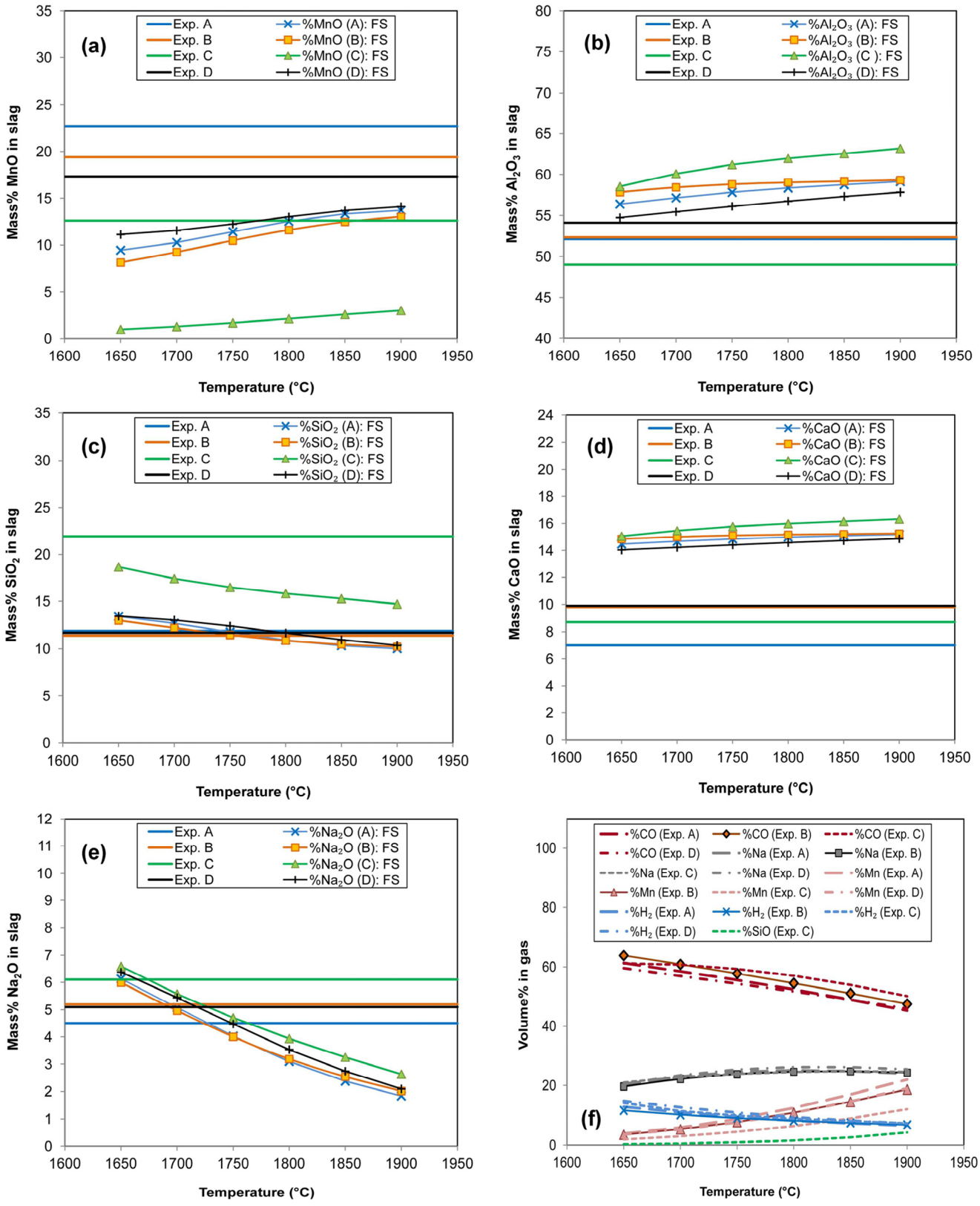

Figure 5. Gas–slag–metal equilibrium compositions of the slag and gas phase vs. experiment. (**a**) MnO; (**b**) Al_2O_3; (**c**) SiO_2; (**d**) CaO; (**e**) Na_2O; (**f**) Gas composition.

The equilibrium calculation results in Figures 4 and 5 are informative, but only hint at the most critical reactions. Clearly, Reaction (1) plays the leading role in the overall process, but other reduction reactions also influence the process equilibrium. For example, the

reducing gases CO and H_2 likely also assist in maintaining reducing conditions. A more accurate comparison of the relative influence of each reductant is shown in Figure 6a–d. The g–s–m equilibrium calculation partial oxygen pressure (P_{O_2}) and the P_{O_2} values calculated for the endpoint slag and alloy activities, as shown in Figure 2 and Appendix A, are compared. The P_{O_2} values were calculated from the equilibrium constants of reduction Reactions (11)–(15) and compared to the g–s–m equilibrium P_{O_2} values as displayed in Figure 6a–d and summarised in Appendix C, Tables A6–A9.

$$2(\underline{Al}) + 3/2[O_2] = (\underline{Al_2O_3}) \quad (11)$$

$$(\underline{Mn}) + 1/2[O_2] = (\underline{MnO}) \quad (12)$$

$$(\underline{Si}) + [O_2] = (\underline{SiO_2}) \quad (13)$$

$$(\underline{Cr}) + 1/2[O_2] = (\underline{CrO}) \quad (14)$$

$$(\underline{C}) + 1/2[O_2] = [CO] \quad (15)$$

< > = solid; ( ) = liquid; [ ] = gas; underlined compound indicates it is in solution.

Figure 6a shows that the g–s–m equilibrium P_{O_2} values coincide with the C/CO reaction P_{O_2} values in the temperature interval under consideration, 1650 °C to 1900 °C, if the P_{CO} is set to 1. However, if the P_{CO} is set to 0.5 atm, this overlap no longer holds. Therefore, the importance of Reaction (15) seems limited in setting the reaction system P_{O_2}. Interestingly, at 1650 °C and 1700 °C, the g–s–m equilibrium P_{O_2} values also coincide with the Si/SiO_2 and the Mn/MnO reaction P_{O_2} values. Similarly, at 1850 °C and 1900 °C, the g–s–m equilibrium P_{O_2} values coincide with the Al/Al_2O_3 reaction P_{O_2} values.

In Figure 6b the g–s–m equilibrium P_{O_2} values overlap at all of the considered temperatures with the Si/SiO_2 reaction P_{O_2} values, indicating that this reaction sets the system's reduction-potential conditions. In contrast, in Figure 6c with added silicon collector metal, there is no such overlap with the g–s–m equilibrium P_{O_2} values. This is an unexpected trend, as the added silicon should readily influence the system's reduction potential, given the predicted uptake of alloy silicon in the g–s–m simulation. In Figure 6d there is an overlap between the g–s–m equilibrium P_{O_2} values and the Cr/CrO reaction P_{O_2} values at 1750 °C to 1900 °C, also coinciding with the Mn/MnO reaction P_{O_2} values at 1850 °C to 1900 °C. Although Cr has a much lower oxygen affinity than Mn, Si, and Al, it appears to participate in setting the system P_{O_2}.

The alloy stability diagrams displayed in Figure 7a–d were constructed to test the sensitivity of alloy aluminium content to the P_{O_2} for each alloy composition and with 1800 °C as the input temperature. Diamond icons were added to the diagrams to mark the coordinates of the experimental %Al values from Table 3 versus the P_{O_2} value for the Al/Al_2O_3 Reaction (11) as displayed in Appendix C in Tables A6–A9.

For comparison, the g–s–m equilibrium P_{O_2} values and matching %Al values are indicated as circle icons. It is seen that the icons lie on or close to the (LIQUID alloy)–(M_2O_3 corundum + LIQUID) boundary line, indicating P_{O_2} control via Reaction (11) for the oxide phase as corundum (Al_2O_3), equivalent to an alumina-saturated slag. Therefore, the slag phase may not be at equilibrium as time is required to dissolve all the Al_2O_3 into the slag glass phase, indicated by square icons. The higher %Al in the experimental alloys compared with the equilibrium %Al values indicates direct uptake of the aluminium reductant into the alloys.

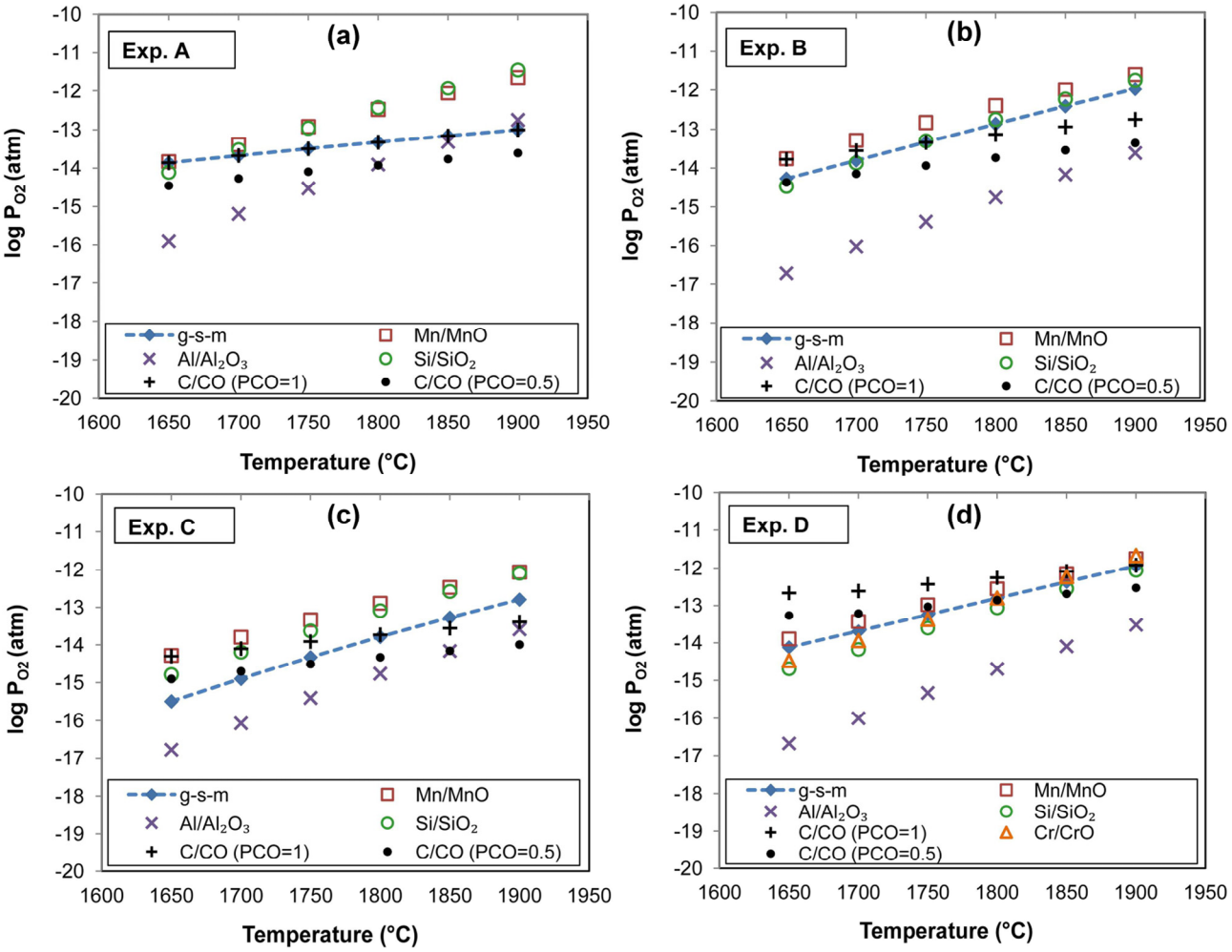

Figure 6. Partial oxygen pressure (P_{O_2}) values of Reactions (11)–(15) at endpoint activity values versus gas–slag–metal equilibrium (g–s–m) P_{O_2} values. (**a**) sample A; (**b**) sample B; (**c**) sample C; (**d**) sample D.

Table 7 presents the manganese yields from the experiments, compared with the g–s–m equilibrium values at 1700 °C, 1800 °C, and 1900 °C. The g–s–m equilibrium values decrease with increased temperature due to loss of metal via volatilisation. The g–s–m equilibrium-predicted manganese yield values for samples A, B and D are similar, but only the sample D experimental value corresponds to the equilibrium-predicted value for the 1900 °C equilibrium. The equilibrium values for sample C with the addition of silicon collector metal are much higher, as only 2% MnO is predicted to remain in the slag.

Table 7. Manganese yield comparison.

Mixture	%Mn to Alloy	g–s–m Equilibrium at 1700 °C	g–s–m Equilibrium at 1800 °C	g–s–m Equilibrium at 1900 °C
A	33	78	67	50
B	42	80	70	56
C	51	96	91	82
D	53	77	68	55

In summary, the g–s–m equilibrium calculation, as applied in this work to the SHS simulation, provides a helpful guide to the overall process and provides ballpark estimates of elemental distributions for the cases of no collector metal, copper collector metal addition,

and chromium collector metal addition. Significant differences exist in the application of silicon collector metal addition.

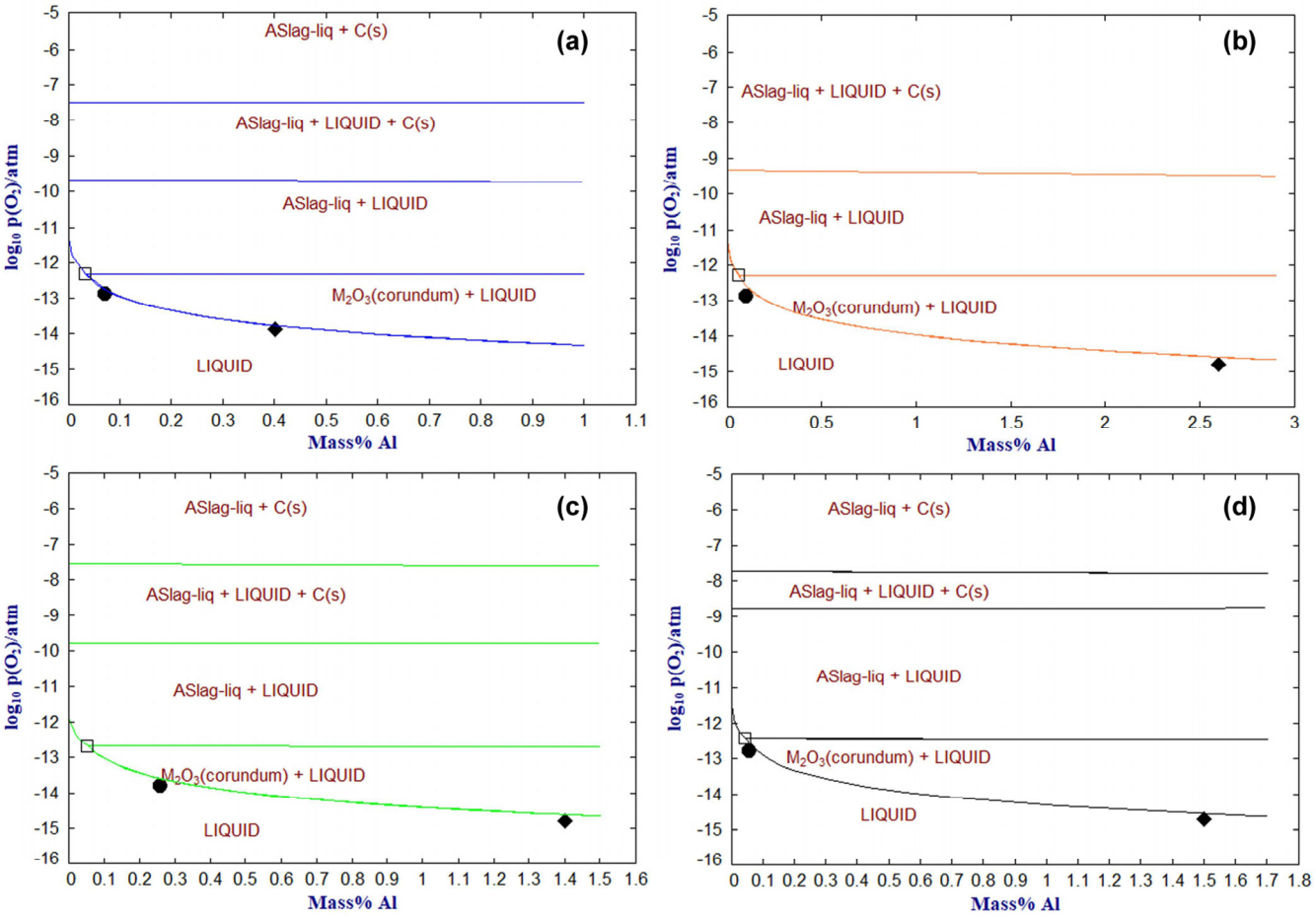

Figure 7. Alloy equilibrium partial oxygen pressure values versus %Al for each alloy composition in Table 3, at 1800 °C. (**a**) sample A; (**b**) sample B; (**c**) sample C; (**d**) sample D. Diamonds = $\log(P_{O_2})$ values for Al/Al_2O_3 Reaction (11) at experiment %Al; circles = g–s–m $\log(P_{O_2})$ vs. %Al values; squares = Al_2O_3–slag–alloy equilibrium intercept. M_2O_3 (corundum) = 99.9% Al_2O_3.

5. Conclusions

This work assesses gas–slag–metal equilibrium calculations in the modelling of sodium-oxide fluxed aluminothermic reduction of pyrolusite-based manganese ore under self-propagating high-temperature synthesis (SHS) conditions. Process variations include the use of different collector metals, such as Si, Cr, and Cu. The main findings are:

- Discrepancies between experimental and equilibrium results highlight the kinetic factors of SHS processes, particularly with respect to aluminium uptake and manganese volatilisation.
- The main difference is the alloy aluminium content. The difference between the calculated and experimental aluminium levels is, in part, due to the higher partial oxygen pressure predicted in the gas–slag–metal equilibrium calculations, compared with that of the Al–Al_2O_3 governing reaction equilibrium. Short-circuiting of aluminium to the alloy is also possible.
- The gas–slag–metal equilibrium calculation provides a helpful guide in process chemistry design and provides ballpark estimates of elemental distributions, although not precise in the aluminium uptake to the alloy.

Author Contributions: F.D.B. conceptualised the experimental work. F.D.B. and T.C. executed the experiments together, interpreted the data together, and prepared the manuscript together. T.C. made the model calculations. All authors have read and agreed to the published version of the manuscript.

Funding: This research was funded in part by the University of Pretoria.

Data Availability Statement: The original contributions presented in this study are included in the article. Further inquiries can be directed to the corresponding author.

Acknowledgments: The authors are grateful to Coenraad Snyman at the Laboratory for Microscopy and Microanalysis at the University of Pretoria for his advice and assistance with analytical techniques.

Conflicts of Interest: The authors declare no conflicts of interest. The funders had no role in the design of the study; in the collection, analyses, or interpretation of data; in the writing of the manuscript, or in the decision to publish the results.

Abbreviations

The following abbreviations are used in this manuscript:

TMF	Thermodynamically most-favoured
g–s–m	Gas–slag–metal
SHS	Self-propagating high-temperature synthesis
FCAW–S	Self-shielded flux-cored arc welding
SAW	Submerged arc welding
AT	Adiabatic temperature

Appendix A

Table A1. Sample A alloy and slag endpoint activities.

Temperature (°C)	aMnO	$aSiO_2$	aAl_2O_3	aMn	aSi	aAl	aC
1650	1.13×10^{-1}	6.98×10^{-3}	2.80×10^{-1}	4.81×10^{-1}	3.75×10^{-4}	3.53×10^{-3}	2.71×10^{-3}
1700	1.08×10^{-1}	7.80×10^{-3}	3.14×10^{-1}	4.50×10^{-1}	4.69×10^{-4}	3.74×10^{-3}	3.17×10^{-3}
1750	1.08×10^{-1}	8.53×10^{-3}	3.20×10^{-1}	4.50×10^{-1}	5.80×10^{-4}	3.95×10^{-3}	3.68×10^{-3}
1800	1.09×10^{-1}	9.27×10^{-3}	3.26×10^{-1}	4.50×10^{-1}	7.11×10^{-4}	4.16×10^{-3}	4.25×10^{-3}
1850	1.10×10^{-1}	1.00×10^{-2}	3.31×10^{-1}	4.49×10^{-1}	8.62×10^{-4}	4.37×10^{-3}	4.87×10^{-3}
1900	1.10×10^{-1}	1.08×10^{-2}	3.35×10^{-1}	4.49×10^{-1}	1.04×10^{-3}	4.59×10^{-3}	5.54×10^{-3}

Table A2. Sample B alloy and slag endpoint activities.

Temperature (°C)	aMnO	$aSiO_2$	aAl_2O_3	aMn	aSi	aAl	aC	aCu
1650	1.14×10^{-1}	4.67×10^{-3}	2.44×10^{-1}	4.16×10^{-1}	5.79×10^{-4}	1.32×10^{-2}	2.45×10^{-3}	3.44×10^{-1}
1700	1.13×10^{-1}	5.14×10^{-3}	2.53×10^{-1}	4.18×10^{-1}	6.98×10^{-4}	1.42×10^{-2}	2.75×10^{-3}	3.36×10^{-1}
1750	1.12×10^{-1}	5.63×10^{-3}	2.62×10^{-1}	4.20×10^{-1}	8.32×10^{-4}	1.53×10^{-2}	3.07×10^{-3}	3.28×10^{-1}
1800	1.12×10^{-1}	6.12×10^{-3}	2.69×10^{-1}	4.22×10^{-1}	9.84×10^{-4}	1.64×10^{-2}	3.41×10^{-3}	3.21×10^{-1}
1850	1.11×10^{-1}	6.62×10^{-3}	2.77×10^{-1}	4.24×10^{-1}	1.16×10^{-3}	1.76×10^{-2}	3.76×10^{-3}	3.15×10^{-1}
1900	1.11×10^{-1}	7.13×10^{-3}	2.84×10^{-1}	4.26×10^{-1}	1.35×10^{-3}	1.88×10^{-2}	4.14×10^{-3}	3.08×10^{-1}

Table A3. Sample C alloy and slag endpoint activities.

Temperature (°C)	aMnO	$aSiO_2$	aAl_2O_3	aMn	aSi	aAl	aC
1650	5.25×10^{-2}	2.97×10^{-2}	2.65×10^{-1}	3.52×10^{-1}	7.64×10^{-3}	1.55×10^{-2}	4.51×10^{-3}
1700	5.30×10^{-2}	3.14×10^{-2}	2.74×10^{-1}	3.55×10^{-1}	8.98×10^{-3}	1.61×10^{-2}	5.21×10^{-3}
1750	5.37×10^{-2}	3.31×10^{-2}	2.81×10^{-1}	3.58×10^{-1}	1.05×10^{-2}	1.67×10^{-2}	5.97×10^{-3}
1800	5.43×10^{-2}	3.48×10^{-2}	2.88×10^{-1}	3.60×10^{-1}	1.21×10^{-2}	1.73×10^{-2}	6.80×10^{-3}
1850	5.50×10^{-2}	3.65×10^{-2}	2.95×10^{-1}	3.62×10^{-1}	1.39×10^{-2}	1.79×10^{-2}	7.69×10^{-3}
1900	5.57×10^{-2}	3.82×10^{-2}	3.00×10^{-1}	3.65×10^{-1}	1.59×10^{-2}	1.85×10^{-2}	8.65×10^{-3}

Table A4. Sample D alloy and slag endpoint activities.

Temperature (°C)	aMnO	$aSiO_2$	aAl_2O_3	aMn	aSi	aAl	aC	aCr	aCrO
1650	1.07×10^{-1}	4.47×10^{-3}	2.65×10^{-1}	4.57×10^{-1}	9.12×10^{-4}	1.30×10^{-2}	6.84×10^{-4}	1.40×10^{-1}	5.53×10^{-3}
1700	1.05×10^{-1}	4.91×10^{-3}	2.76×10^{-1}	4.61×10^{-1}	1.34×10^{-3}	1.42×10^{-2}	9.34×10^{-4}	1.44×10^{-1}	6.56×10^{-3}
1750	1.04×10^{-1}	5.35×10^{-3}	2.85×10^{-1}	4.62×10^{-1}	1.61×10^{-3}	1.49×10^{-2}	1.08×10^{-3}	1.46×10^{-1}	8.14×10^{-3}
1800	1.03×10^{-1}	5.80×10^{-3}	2.95×10^{-1}	4.64×10^{-1}	1.91×10^{-3}	1.55×10^{-2}	1.24×10^{-3}	1.48×10^{-1}	1.04×10^{-2}
1850	1.02×10^{-1}	6.25×10^{-3}	3.03×10^{-1}	4.65×10^{-1}	2.24×10^{-3}	1.61×10^{-2}	1.41×10^{-3}	1.50×10^{-1}	1.35×10^{-2}
1900	1.02×10^{-1}	6.70×10^{-3}	3.11×10^{-1}	4.67×10^{-1}	2.62×10^{-3}	1.68×10^{-2}	1.60×10^{-3}	1.51×10^{-1}	1.75×10^{-2}

Appendix B

Table A5. Sample A Gibbs free energy values for Reaction (1).

Temperature (°C)	ΔG° (kJ/mol Al)	#1: Worst-Case Scenario ΔG (kJ/mol Al)	K for Scenario #1	#2: Most Favourable Scenario ΔG (kJ/mol Al)	K for Scenario #2
1650	−170.5	−57.3	1189.1	−199.8	0.160
1700	−168.3	−51.0	1280.6	−197.5	0.169
1750	−166.2	−46.8	1212.7	−195.9	0.171
1800	−161.9	−42.6	1149.4	−194.4	0.172
1850	−159.8	−38.5	1090.3	−192.9	0.173
1900	−155.7	−34.4	1035.2	−191.4	0.174

Appendix C

Table A6. Sample A: log (P_{O_2}) values as displayed in Figure 6a.

Temperature (°C)	Reaction (11): Al/Al_2O_3	Reaction (12): Mn/MnO	Reaction (13): Si/SiO_2	Reaction (15): C/CO; P_{CO} = 1.0	Reaction (15): C/CO; P_{CO} = 0.5	g–s–m
1650	−15.9	−13.8	−14.1	−13.9	−14.5	−14.3
1700	−15.2	−13.4	−13.5	−13.7	−14.5	−13.8
1750	−14.5	−12.9	−13.0	−13.5	−14.1	−13.4
1800	−13.9	−12.5	−12.4	−13.3	−13.9	−12.9
1850	−13.3	−12.1	−11.9	−13.2	−13.8	−12.5
1900	−12.7	−11.6	−11.4	−13.0	−13.6	−12.1

Table A7. Sample B: log (P_{O_2}) values as displayed in Figure 6b.

Temperature (°C)	Reaction (11): Al/Al_2O_3	Reaction (12): Mn/MnO	Reaction (13): Si/SiO_2	Reaction (15): C/CO; P_{CO} = 1.0	Reaction (15): C/CO; P_{CO} = 0.5	g–s–m
1650	−16.7	−13.8	−14.5	−13.8	−14.4	−14.3
1700	−16.0	−13.3	−13.9	−13.5	−14.1	−13.8
1750	−15.4	−12.8	−13.3	−13.3	−13.9	−13.3
1800	−14.8	−12.4	−12.8	−13.1	−13.7	−12.9
1850	−14.2	−12.0	−12.2	−12.9	−13.5	−12.4
1900	−13.6	−11.6	−11.7	−12.7	−13.4	−12.0

Table A8. Sample C: log (P_{O_2}) values as displayed in Figure 6c.

Temperature (°C)	Reaction (11): Al/Al_2O_3	Reaction (12): Mn/MnO	Reaction (13): Si/SiO_2	Reaction (15): C/CO; P_{CO} = 1.0	Reaction (15): C/CO; P_{CO} = 0.5	g–s–m
1650	−16.8	−14.3	−14.8	−14.3	−14.9	−15.5
1700	−16.1	−13.8	−14.2	−14.1	−14.7	−14.9
1750	−15.4	−13.3	−13.6	−13.9	−14.5	−14.3
1800	−14.8	−12.9	−13.1	−13.7	−14.3	−13.8
1850	−14.2	−12.5	−12.6	−13.6	−14.2	−13.3
1900	−13.6	−12.1	−12.1	−13.4	−14.0	−12.8

Table A9. Sample D: log (P_{O_2}) values as displayed in Figure 6d.

Temperature (°C)	Reaction (11): Al/Al_2O_3	Reaction (12): Mn/MnO	Reaction (13): Si/SiO_2	Reaction (15): C/CO; P_{CO} = 1.0	Reaction (15): C/CO; P_{CO} = 0.5	g–s–m	Reaction (14): Cr/CrO
1650	−16.7	−13.9	−14.7	−12.7	−13.3	−14.1	−14.5
1700	−16.0	−13.4	−14.2	−12.6	−13.2	−13.7	−13.9
1750	−15.3	−13.0	−13.6	−12.4	−13.0	−13.2	−13.4
1800	−14.7	−12.6	−13.1	−12.3	−12.9	−12.8	−12.8
1850	−14.1	−12.1	−12.5	−12.1	−12.7	−12.4	−12.2
1900	−13.5	−11.8	−12.1	−11.9	−12.5	−11.9	−11.7

References

1. Azof, F.I.; Safarian, J. Leaching kinetics and mechanism of slag produced from smelting–reduction of bauxite for alumina recovery. *Hydrometallurgy* **2020**, *195*, 105388. [CrossRef]
2. Pilla, G.; Hertel, T.; Pontikes, Y. Toward an integrated and sustainable Bauxite residue valorization, employing H_2 reduction roasting, carbonation, and bio–carbon smelting. *J. Sustain. Metall.* **2025**, *11*, 1745–1765. [CrossRef]
3. Sparis, D.; Lazou, A.; Balomenos, E.; Panias, D. Thermodynamics of Aluminothermic Processes for Ferrotitanium Alloy Production from Bauxite Residue and Ilmenite. *Metals* **2024**, *14*, 200. [CrossRef]
4. Komarov, O.N.; Zhilin, S.G. Formation of alloy chemical composition produced by aluminothermy on alloying with tungsten extracted from scheelite concentrate. *Metallurgist* **2022**, *65*, 995–1007. [CrossRef]
5. Barsukova, N.V.; Popov, A.V.; Komarov, O.N. Evolution of structure and properties of iron–carbon alloys produced by aluminothermy at differentiation of fractional composition of charge materials. *Metallurgist* **2025**, *68*, 1743–1755. [CrossRef]
6. Barsukova, N.V.; Komarov, O.N.; Zhilin, S.G.; Predein, V.V.; Popov, A.V.; Khudyakova, V.A. Control of Properties of Iron–Carbon Alloys Produced by Aluminothermy by Varying Technological Factors. *Metallurgist* **2023**, *67*, 1192–1207. [CrossRef]
7. Kudyba, A.; Akhtar, S.; Johansen, I.; Safarian, J. Aluminothermic Reduction of Manganese Oxide from Selected MnO–Containing Slags. *Materials* **2021**, *14*, 356. [CrossRef]
8. Kudyba, A.; Safarian, J. Manganese and Aluminium Recovery from Ferromanganese Slag and Al White Dross by a High Temperature Smelting–Reduction Process. *Materials* **2022**, *15*, 405. [CrossRef] [PubMed]
9. Philipson, H.; Wallin, M.; Einarsrud, K.E.; Tranell, G. Kinetics of silicon production by aluminothermic reduction of silica using aluminum and aluminum dross as reductants. In Proceedings of the 16th International Ferro-Alloys Congress (INFACON XVI), Virtual, 27–29 September 2021; NTNU: Trondheim, Norway, 2021.

10. Philipson, H.G.R.; Wallin, M.; Einarsrud, K.E. Investigation of Liquid–Liquid Reaction Phenomena of Aluminum in Calcium Silicate Slag. *Materials* **2024**, *17*, 1466. [CrossRef]
11. Bhoi, B.; Murthy, B.V.R.; Datta, P.; Rajeev; Jouhari, A.K. Studies on Aluminothermic Reduction of Manganese ore for Ferro Manganese Making. In *Proceeding: Ferro Alloy Industries in the Liberalised Economy*; Vatsh, A.K., Singh, S.D., Goswami, N.G., Ramachandrarao, P., Eds.; NML: Jainshedpur, India, 1997; pp. 66–70.
12. Nababan, D.C.; Mukhlis, R.; Durandet, Y.; Prentice, L.H.; Rickard, W.D.A.; Pownceby, M.I.; Rhamdani, M.A. Recycling of $LiCoO_2$ Battery Cathode Material Through Aluminothermic Reduction Using Aluminum Waste Chips. *Met. Mater. Trans. B* **2024**, *55*, 144–167. [CrossRef]
13. Makhambetov, Y.; Abdulina, S.; Kabylkanov, S.; Burumbayev, A.; Zhakan, A.; Sadyk, Z.; Akhmetov, A. Production of Chromium–Manganese Ligature from Low–Grade Chromium and Iron–Manganese Ores Using Silicon—Aluminum Alloys as Reductants. *Processes* **2025**, *13*, 3158. [CrossRef]
14. Merzhanov, A.G. Problems of combustion in chemical technology and in metallurgy. *Russ. Chem. Rev.* **1976**, *45*, 409–420. [CrossRef]
15. Mossino, P. Some aspects in self–propagating high–temperature synthesis. *Ceram. Int.* **2004**, *30*, 311–332. [CrossRef]
16. Song, J.; Guo, T.; Dine, W.; Yang, L.; Zhang, X.; Yu, Z.; Wu, J.; Zhang, J.; Fang, X. The effect of Al particle size on the thermal behvior and kinetics of Al–MnO_2 thermite system. *Adv. Mater. Sci. Eng.* **2020**, *2020*, 3097404. [CrossRef]
17. Sarangi, B.; Sarangi, A.; Ray, H.S. Kinetics of aluminothermic reduction of MnO_2 and Fe_2O_3: A thermoanalytical investigation. *ISIJ Int.* **1996**, *36*, 1135–1141. [CrossRef]
18. Andrusev, M.M. 150 Years since the birth of the eminent Russian physical chemist and metallurgist N.N. Beketov. *Metallurgist* **1977**, *21*, 416–418. [CrossRef]
19. Coetsee, T.; De Bruin, F. Sodium Oxide–Fluxed Aluminothermic Reduction of Manganese Ore with Synergistic Effects of C and Si Reductants: SEM Study and Phase Stability Calculations. *Reactions* **2025**, *6*, 40. [CrossRef]
20. Coetsee, T.; De Bruin, F. Sodium–Oxide Fluxed Aluminothermic Reduction of Manganese Ore for a Circular Economy: Cr Collector Metal Application. *Sustain. Chem.* **2025**, *6*, 30. [CrossRef]
21. Coetsee, T.; De Bruin, F. Investigation of Copper as Collector Metal in Sodium-Oxide Fluxed Aluminothermic Reduction of Manganese Ore. *Crystals* **2026**, *16*, 50. [CrossRef]
22. Rafiei, M.; Ahmadnezhad, M.; Mostaan, H.; Saeidi, A. Reaction mechanism in SiO_2–MnO_2–Fe–Al system for producing ferrosiliconmanganese powder. *Adv. Powder Technol.* **2020**, *31*, 2613–2617. [CrossRef]
23. Yang, J.; Kuwabara, M.; Sawada, T.; Sano, M. Kinetics of isothermal reduction of MgO with Al. *ISIJ Int.* **2006**, *46*, 1130–1136. [CrossRef]
24. Trembach, B.; Trembach, I.; Grin, A.; Makarenko, N.; Babych, O.; Knyazev, S.; Musairova, Y.; Krbata, M.; Balenko, O.; Vorobiov, O.; et al. Study of the Effects of Hardfacing Modes Carried out by FCAW–S with Exothermic Addition of MnO_2–Al on Non–Metallic Inclusions, Grain Size, Microstructure and Mechanical Properties. *Eng* **2025**, *6*, 125. [CrossRef]
25. Trembach, B.; Silchenko, Y.; Balenko, O.; Hlachev, D.; Kulahin, K.; Heiko, H.; Bellorin-Herrera, O.; Khabosha, S.; Zakovorotnyi, O.; Trembach, I. Study of the hardfacing process using self-shielding flux-cored wire with an exothermic addition with a combined oxidizer of the Al-(CuO/Fe_2O_3) system. *Int. J. Adv. Manuf. Technol.* **2024**, *134*, 309–335. [CrossRef]
26. Trembach, B.; Trembach, I.; Maliuha, V.; Knyazev, S.; Krbata, M.; Kabatskyi, O.; Balenko, O.; Zarichniak, Y.; Brechka, M.; Mykhailo, B.; et al. Study of self-shielded flux-cored wire with exothermic additions CuO-Al on weld bead morphology, microstructure, and mechanical properties. *Int. J. Adv. Manuf. Technol.* **2025**, *137*, 4685–4711. [CrossRef]
27. Coetsee, T.; De Bruin, F. Application of Copper as Stabiliser in Aluminium Assisted Transfer of Titanium in Submerged Arc Welding of Carbon Steel. *Processes* **2021**, *9*, 1763. [CrossRef]
28. Bale, C.W.; Bélisle, E.; Chartrand, P.; Decterov, S.A.; Eriksson, G.; Gheribi, A.E.; Hack, K.; Jung, I.-H.; Kang, Y.-B.; Melançon, J.; et al. FactSage thermochemical software and databases, 2010–2016. *Calphad* **2016**, *54*, 35–53, Reprinted in *Calphad* **2016**, *55*, 1–19. [CrossRef]
29. Habashi, F. (Ed.) *Handbook of Extractive Metallurgy*; Wiley-VCH: Weinheim, Germany, 1997; Volume 1, pp. 420–451.
30. Anderson, J.R. Solubility of Carbon in Molten Copper–Manganese and Copper–Nickel Alloys. Master's Thesis, Massachusetts Institute of Technology, Cambridge, MA, USA, 1946; p. 14.
31. Gaskell, D.R. *Introduction to Metallurgical Thermodynamics*, 2nd ed.; Hemisphere Publishing Corporation: New York, NY, USA, 1981; p. 287.